Identification of Pauses during Formation of HIV-1 Virus Like Particles

Pei-I Ku,[†‡] Anna K. Miller,[§] Jeff Ballew,[¶] Virginie Sandrin,[||] Frederick R. Adler,[§**] and Saveez Saffarian[†‡***]
[†]Department of Physics and Astronomy, [‡]Center for Cell and Genome Science, and [§]Department of Mathematics, University of Utah, Salt Lake City, Utah; [¶]Department of Biology, Utah Valley University, Orem, Utah; and [||]Biochemistry Department and **Department of Biology, University of Utah, Salt Lake City, Utah

ABSTRACT HIV Gag polymerizes on the plasma membrane to form virus like particles (VLPs) that have similar diameters to wild-type viruses. We use multicolor, dual-penetration depth, total internal reflection fluorescence microscopy, which corrects for azimuthal movement, to image the assembly of individual VLPs from the time of nucleation to the recruitment of VPS4 (a component of the endosomal sorting complexes required for transport, and which marks the final stage of VLP assembly). Using a mathematical model for assembly and maximum-likelihood comparison of fits both with and without pauses, we detect pauses during Gag polymerization in 60% of VLPs. Pauses range from 2 to 20 min, with an exponentially distributed duration that is independent of cytosolic Gag concentration. VLPs assembled with late domain mutants of Gag (which do not recruit the key endosomal sorting complexes required for transport proteins Alix or TSG101) exhibit similar pause distributions. These pauses indicate that a single rate-limiting event is required for continuation of assembly. We suggest that pauses are either related to incorporation of defects in the hexagonal Gag lattice during VLP assembly or are caused by shortcomings in interactions of Gag with essential and still undefined cellular components during formation of curvature on the plasma membrane.

INTRODUCTION

HIV Gag polymerization on the plasma membrane drives the budding of HIV particles. How the polymerization of Gag is linked to the creation of membrane curvature, and what (if any) cellular proteins are involved during the formation of curvature, remains unclear. Gag consists of three folded domains, MA, CA, and NC, and three unstructured regions, SP1, SP2, and P6 (1). The MA domain is essential for targeting Gag onto the inner leaflet of the plasma membrane, and contains a PIP2 binding site as well as a myristoylation motif, which contributes to membrane binding. The CA domains in adjacent Gag proteins bind each other with strong affinity and these interactions are critical for hexagonal arrangements of Gag within immature HIV virions as observed by cryo-electron microscopy (cryo-EM) (2,3). To catalyze the fission of the host membrane and the release of the virus, endosomal sorting complexes required for transport (ESCRTs) (4–8) recruit to the HIV assembly site, culminating in arrival of the AAA ATPase VPS4 (9).

HIV Gag alone is sufficient to create fully formed vesicles coated with Gag that bud into the extracellular space as virus like particles (VLPs) (1), but so far attempts to reconstitute the formation of VLPs in vitro from purified components have not been successful. Although we know that HIV virions are enriched in well-ordered lipid domains and cholesterol (10–12), the exact mechanism by which these lipids become enriched in the forming VLP is not clear (9,13). Therefore, aside from Gag polymerization, lipid and protein interactions on the inner leaflet of the plasma membrane play a clear role in assembly of HIV virions.

In the immature HIV virion, Gag forms an incomplete lattice of hexagonal geometry on the inner leaflet of the plasma membrane held together mainly through CA-CA interactions. In the mature HIV, the CA domains are cleaved and the HIV core is assembled through CA-CA interactions (14,15). The HIV core incorporates 12 pentagons to ensure forming a closed shell (14). Cryo-EM measurements of the immature HIV virions, however, revealed no pentagonal facets within the lattice. Therefore, to create a closed topology, the immature virion incorporates empty patches as defects within the hexagonal lattice (2,16,17). These defects could be the results of membrane fission (17). However, before the fission of the membrane, the hexagonal lattice of Gag needs to curve, which requires deviations from hexagonal lattice assembly. These observations suggest a complex relationship between Gag polymerization and membrane curvature during virion formation, which would likely manifest itself in the kinetics of assembly.

Assembly of individual HIV VLPs has been observed using total internal reflection fluorescence (TIRF) microscopy. These studies show that formation of HIV VLP initiates at the plasma membrane and continues through

Submitted April 14, 2013, and accepted for publication September 24, 2013.

*Correspondence: saffarian@physics.utah.edu

Pei-I Ku and Anna K. Miller contributed equally to this article.

Editor: David Piston.

0006-3495/13/11/2262/11 $2.00

http://dx.doi.org/10.1016/j.bpj.2013.09.047

polymerization of Gag, resulting in fully formed HIV virions (18,19). A vector system that expresses wild-type levels of Gag and Gag-Pol proteins (18) showed the same kinetics for assembly as transient transfection of Gag and Gag-mCherry (19). Therefore, the presence of Gag-Pol or fluorescent protein fusions were shown to have minimal effects on the kinetics of assembly.

Recruitment of ESCRT proteins into forming HIV VLPs was observed using dual-color TIRF microscopy (20,21). The two late ESCRT factors CHMP4 and VPS4 protein are transiently recruited to the VLP for 25–30 s at the last step after Gag polymerization is complete (20). The arrival of ESCRT proteins is a molecular signature for the release of VLPs. Because the resolution of optical microscopy is limited, before visualization of ESCRT recruitment, the fully formed VLP was inferred either through a plateau in Gag polymerization followed by subsequent movement of the VLP (18), or through incorporation and subsequent quenching of pH-sensitive fluorescent proteins fused to Gag at the end of the imaging period (19).

The kinetics of assembly of HIV VLPs have been studied in the context of late domain mutants of Gag. Within the P6 domain of HIV Gag, there are two conserved L domain motifs: 1), a PTAP motif that functions as the primary HIV-1 binding site to ESCRT-I component Tsg101 (4,5,9,22); and 2), a LYPxL motif that binds to ALIX, an auxiliary member of the ESCRT pathway (7,8). Gag double mutants lacking functional PTAP and LYPxL motifs were shown to have identical kinetics to wild-type Gag during assembly of HIV VLPs (18,19). Aside from TSG101 and Alix, ubiquitin ligases have been shown to play a role in the budding of HIV (24–26). Unlike TSG101 and Alix (which are believed to be mostly involved in the last stage of VLP formation with almost no effect on the kinetics of assembly), it is not clear how the ubiquitination of Gag affects the kinetics of assembly.

Assembly of HIV VLPs is driven by polymerization of Gag on the inner leaflet of the plasma membrane. Gag molecules interact with each other and with the plasma membrane, and possibly with the cellular machinery during this polymerization. Exactly how the polymerization of Gag is linked to the creation of membrane curvature and what, if any, cellular components are involved during the formation of curvature, is not clear. The ESCRT machinery, which is the most well-characterized partner of Gag, is mostly engaged during the end stages of the VLP formation and its separation from the host cell. Because Gag polymerization is the primary driver of the VLP formation and there is an abundance of Gag within the cytosol during polymerization, the polymerization of Gag on the membrane during VLP formation should be able to proceed uninterrupted. Through monitoring the accumulation of fluorescence from fluorescently tagged Gag molecules within a forming VLP, the polymerization kinetics of Gag has been previously established (18,19). However, the previous measurements were performed using TIRF microscopy and therefore it has been difficult to relate the fluorescence directly to Gag incorporation. This is because fluorescence could be affected both by azimuthal movement of the VLP and by accumulation of Gag. Here we have used a method based on dual-penetration depth TIRF microscopy, which allows decoupling of the relative amount of Gag incorporation from azimuthal movements of the VLP. Our measurements of the relative Gag incorporation during the assembly are consistent with previous observations based on single-penetration depth TIRF microscopy; however, we uncovered pauses in the polymerization of Gag at various stages of the VLP formation. These pauses, characterized in this article, are best described as deviations from a simplistic Gag-driven VLP assembly model, and can be caused by possible defects in the organization of Gag within the forming lattice. They can also be caused by shortcomings in interactions of Gag with essential and still undefined cellular components during formation of curvature on the plasma membrane.

MATERIALS AND METHODS

Fusion of VPS4 with fluorescent proteins

Ten DNA constructs were created that encoded the joining of VPS4A to GFP with protein linkages of materially different character. DNA sequences were generated using four helical linkers of similar composition but varying lengths (13, 21, 29, and 37 amino acids) and one flexible linker of 32 amino acids in length. All five linkers were used to generate VPS4A fusions with GFP in both gene orders, e.g., GFP before VPS4A and VPS4A before GFP, for 10 total linkage combinations. The flexible linker avoided helix-forming amino acids.

Testing the functional VPS4 fusions

RNA_i-resistant plasmids of VPS4A fusion with GFP using various linker combinations were used to rescue the knockdown of VPS4A. Production of infectious virus was used as readout for the rescue. This experiment has been described in detail in Morita et al. (27) and in the Supporting Material. Using this test, we found that VPS4A-h37-eGFP (h37 is a 37-amino-acid-long α-helix-forming linker) was the most effective plasmid to rescue the infectivity of HIV-1 produced in cells depleted of endogenous VPS4A and B.

VPS4A-h37-mCherry clonal cell line

HeLa cells were transfected with VPS4A-h37-mCherry plasmid containing a ΔCMV promoter for reduced expression (27). Stable cells were selected through incubation with medium supplemented with 1 mg/mL G418 for a week. After selection, cells were grown and maintained in medium with 0.5 mg/mL G418. Fluorescent cells were then sorted using a cell sorter and diluted into 96-well plates so that each well hosts 1–2 cells. Single colonies were picked up from the 96-well plate after a week and expanded. Colonies were tested for their expression level of VPS4A-h37-mCherry and a single clone was chosen for experiments. This clone has cell-doubling times identical to untransfected control HeLa cells and no cell toxicity was observed.

Cell culture and imaging conditions

The VPS4A-h37-mCherry HeLa clonal cell line was grown in Dulbecco's Modified Eagle's Medium (DMEM; Invitrogen, Carlsbad, CA) with 10% fetal calf serum, sodium pyruvate, and L-glutamine. Cells were seeded 12 h before transfection on sterile 35-mm glass coverslips at 80% confluence. Transfection was carried out using 2 μL of Lipofectamine2000 (Invitrogen) and DNA plasmid mix of 450-ng Gag, 450-ng Gag-eGFP fused Gag, and 100 ng of VPU. Three hours after transfection, the sample was supplemented in CO_2-independent medium plus 2.5% fetal calf serum and moved to the microscope for imaging. The cells were kept at 37°C during the imaging.

Microscope description

Live images were acquired using an iMIC Digital Microscope (TILL Photonics, Gräfelfing, Munich, Germany) controlled with LIVE ACQUISITION imaging software (TILL Photonics). Two laser wavelengths, consisting of a 488-nm diode laser (iBeam Smart 488S; Toptica Photonics, Gräfelfing, Munich, Germany) and a 561-nm diode-pumped solid-state laser (Cobolt Jive, 561-nm Jive High Power; Cobolt, San Jose, CA), were used to excite GFP and mCherry, respectively. Laser beams were passed through an acousto-optical tunable filter and focused onto a fiber that delivered the light to the Yanus Digital Scan Head, utilizing the Polytrope Imaging Mode Switch (equipment by TILL Photonics; see diagram of working setup given in Fig. S2 in the Supporting Material.) The Yanus Digital Scan Head consists of two galvo mirrors and one spherical mirror to control the laser-beam position. The Polytrope Imaging Mode Switch rapidly switches the illumination beam path between the Epi- (wide-field), the FRAP, and the TIRF microscopy modes. It also holds the quadrant photodiode used for TIRF penetration-depth calibration. In the TIRF mode, the Yanus Digital Scan Head (TILL Photonics) is used to control the position of the focused beam in the objective's back focal plane and can be adjusted within 0.2 ms, as shown in Fig. S2. We positioned the focused beam at the edge of the back focal plane of the objective ($N = 1.46$, 100×, Carl Zeiss Microscopy, Thornwood, NY) to reach beyond the critical angle and achieve TIRF. The TIRF critical angle was verified by scanning the laser beam across the back aperture and measuring the reflection of the laser from the glass sample interface back into the objective and onto the quadrant photodiode. The penetration depth of the beam is calculated based on the incident angle of the beam, which is in turn measured by the position of the beam on the quadrant photodiode. Once the penetration depths for the experiments are set at the beginning of acquisition, a feedback loop keeps the focus of the objective on the sample by constantly monitoring the position of the back-reflected beam with respect to the original beam. We also rotated the TIRF illumination on the objective back focal plane at the rate of one turn per exposure (TIRF360) to maximize homogeneity of the TIRF images. We adjusted the laser incident angle and recorded two different penetration-depths' excitation of eGFP(100 and 200 nm, respectively) and one penetration-depth excitation of mCherry (200 nm) every 15 s for 90 min on each cell. The two colors of emission were separated by a Dichrotome Image Splitter (TILL Photonics) and recorded by an electron-multiplying charge-coupled device camera (iXon 897; Andor Technology, Belfast, Ireland). Camera electron-multiplying gain is set at 20, which has been tested to have the best signal/noise. Images were analyzed by a home-written MATLAB algorithm (The MathWorks, Natick, MA), which was previously described in Saffarian and Kirchhausen (28).

Calculating the amount of Gag incorporated in single VLPs forming on the plasma membrane

The intensity of evanescent wave decays exponentially with the distance Z away from the glass and medium interface into the cell sample (29,30). Let Z represent the center-of-mass position of the VLP; I_o the intensity when $Z = 0$ (located at interface surface); and d, the penetration depth. Then,

$$I(z) = I_o e^{-\frac{Z}{d}}. \quad (1)$$

The total TIRF from N Gag-eGFP molecules can be written as

$$F(z) = NqI(z), \quad (2)$$

in which q is a product of quantum yield, absorption coefficient, and the detection efficiency.

To normalize-out the constants, the average intensity of the first 15 data points from the single VLP formation was calculated and used to normalize the fluorescence intensity traces in each of the two penetration-depth Gag-eGFP channels (28). The results yield normalized TIRF fluorescent intensities (F_1 and F_2).

The normalized F_1 and F_2 collected using different penetration-depth illuminations (d_1 and d_2) and the axial position of the center of mass of the VLP can be calculated as

$$Z = \left(\frac{d_1 d_2}{d_2 - d_1}\right)\log\left(\frac{F_2}{F_1}\right). \quad (3)$$

After we calculate Z from Eq. 3, we smooth the noise by a weighted average over time as

$$Z_f = 0.3\,Z_{i-1} + 0.4\,Z_i + 0.3\,Z_{i+1}.$$

Using the position Z_f, we estimate the average Gag-eGFP molecular number inside the VLP as

$$N_i = Fe^{\frac{Z_f}{d_i}}. \quad (4)$$

The relative number of Gag molecules, shown in Fig. 1, is calculated as the average of N_1 and N_2.

To provide insight into VLP assembly, we have also measured the average Z_f position for all VLPs in this study as presented in Fig. S6. The Z_f increases as the VLP assembles, implying that the VLP assembly starts near the glass surface, and further assembly results in an increase to the height of the center of mass of the VLP.

We also measured the differences between N_1 and N_2 during the assembly by calculating $\Delta N/N$. The standard deviation of this value over all of our profiles is 0.074.

Shell-filling model for VLP assembly

We constructed a deterministic model to describe how the total number of Gag proteins would change as the VLP assembles. We incorporate the spherical geometry into the derivation of our model. We first consider how the surface area of a sphere with radius r changes with respect to the polar angle ϕ as shown in Fig. 2, which is given by

$$SA(\phi) = \int_0^{2\pi}\int_0^{\phi} r^2\sin(\phi)d\phi d\theta = 2\pi r^2(1-\cos(\phi)). \quad (5)$$

Not all the VLP is covered with Gag. Indeed, fluorescence fluctuation analysis on purified VLPs has shown a low fraction of Gag coverage within each VLP (31) and cryo-EM of purified immature virions has shown that only ~65% of the surface of the virion is covered with an organized Gag lattice (16). In our model, for the purpose of simplicity, we assumed that the

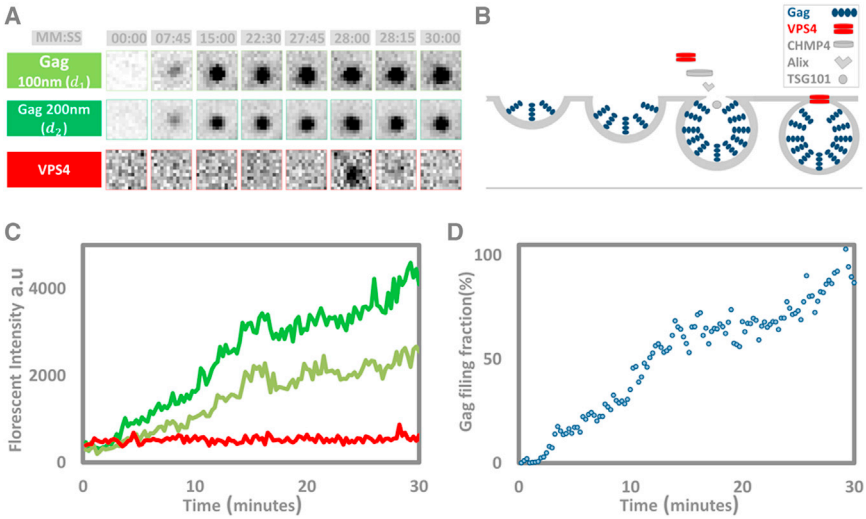

FIGURE 1 Multicolor dual-penetration-depth TIRF microscopy. HeLa cells stably expressing VPS4A-h37-mCherry were transfected with Gag and Gag-eGFP plasmids and imaged 3–7 h post-transfection. (*A*) Assembly of an HIV VLP captured by imaging with 100- and 200-nm TIRF excitation in 488 nm for GFP followed by 200-nm TIRF excitation in 561 nm for mCherry every 15 s. Assembly initiates de novo and concludes with VPS4A recruitment at the end. (*B*) A schematic model of VLP formation and VPS4 recruitment. (*C*) Fluorescence intensity signal from the same VLP as shown in panel *A*. (*D*) The Gag filling fraction calculated for the same traces shown in panel *B* as explained in Materials and Methods. To see this figure in color, go online.

vacancies within the Gag lattice are uniformly distributed and thereby the shell-filling model presented here assumes that the VLP forms a Gag shell with 100% coverage, albeit with a lower packing density. A separate model assuming 65% Gag filling of the VLP is presented in Fig. S3, Fig. S4, and in the Supporting Material text, and shows no effects on the conclusions of our study. We can approximate the surface area of a single Gag protein (SAG) by dividing the total surface area that Gag occupies by the total number of Gag proteins in a single VLP (G_{tot}) as

$$SAG = \frac{4\pi r^2}{G_{\text{tot}}}. \tag{6}$$

Under the assumption that Gag binds only at the cross section of the cell membrane, the total number of Gag proteins (N) at some angle ϕ is

$$N(\phi) = \frac{SA(\phi)}{SAG} = \frac{G_{\text{tot}}}{2}(1-\cos(\phi)). \tag{7}$$

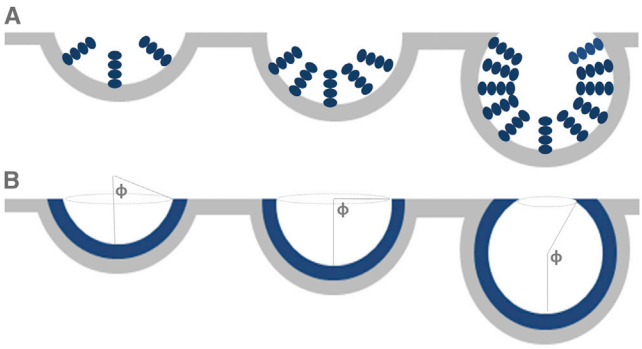

FIGURE 2 Shell-filling model of VLP assembly. (*A*) Gag polymerizes on the plasma membrane to form a VLP. (*B*) We have approximated this process by assuming that new Gag molecules can only join at the periphery of the forming VLP. We also assume that the curvature of the VLP is always identical to the fully formed VLP, therefore parts of the lattice that are built already have the curvature that they would have in the final VLP. To see this figure in color, go online.

In addition, we assume that the polymerization changes the angle ϕ at a constant rate (B). This assumption is governed by the hypothesis that Gag assembly is driven by addition of new Gag monomers to the periphery of the Gag lattice, thereby being proportional to the number of Gag molecules available for binding at the leading ring of the forming HIV-1 particle. Our mathematical model consists of the following system of ordinary differential equations, which is based on an application of the chain rule and the above derivation:

$$\frac{dN}{dt} = \frac{dN}{d\phi}\frac{d\phi}{dt}, \tag{8a}$$

$$\frac{d\phi}{dt} = B. \tag{8b}$$

We assume that the solution to Eq. 8a is proportional to the total intensity (I) of the Gag-GFP, which is given by

$$I(t) = \frac{A}{2}(1-\cos(Bt)). \tag{9}$$

However, the resolution of the image or the filtering of the fluorescence may affect the time at which we begin to detect the fluorescence. To incorporate this into our solution, we start our time t at the time when the VLP becomes visible above noise, but start the shell-filling model at time τ_i (9). This condition means that for most cases, $\tau_1 < 0$, as is shown in Fig. 3. In addition, once the VLP has completely formed, the intensity of the Gag-GFP will reach its maximum (A). Therefore, we define $I(t)$ piecewise as

$$I(t) = \begin{cases} 0 & \text{if} \quad t \le \tau_1 \\ \dfrac{A}{2}(1-\cos(B \times (t-\tau_1))) & \text{if} \quad \tau_1 < t < \dfrac{\pi}{B} + \tau_1 \\ A & \text{if} \quad t \ge \dfrac{\pi}{B} + \tau_1. \end{cases} \tag{10}$$

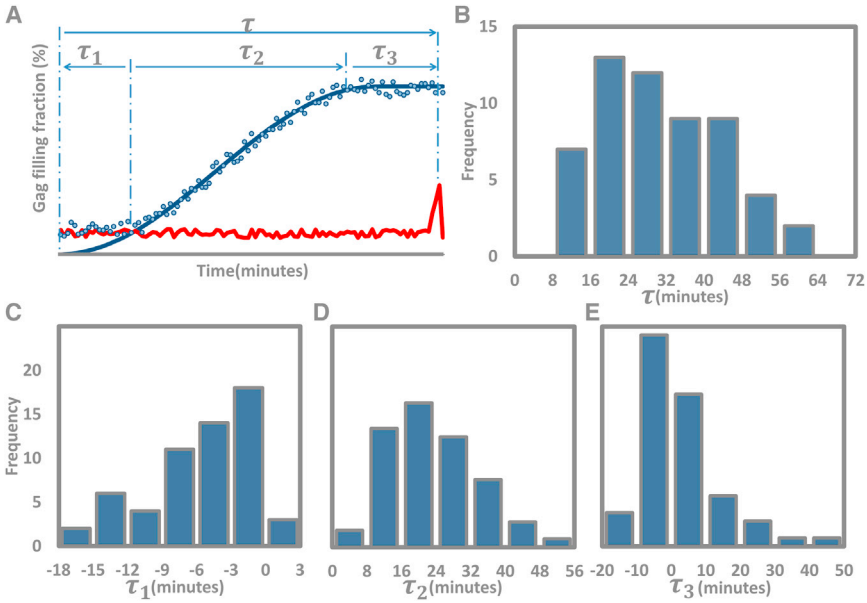

FIGURE 3 Kinetics of VLP formation. (*A*) Definition of various timings on the graph of Gag polymerization (*blue dot*) and VPS4 (*red*) simulated data and Gag polymerization shell-filling model fitting (*blue solid*). We define τ as the VLP formation lifetime, τ_1 as the nucleation time defined by the period of time that Gag VLP had started to assemble but intensity was still below the detection, τ_2 as the Gag polymerization time, and τ_3 as the recruitment time of VPS4 after Gag polymerization was complete. (*B–E*) Histograms of different time periods, τ, τ_1, τ_2, and τ_3 from all 58 VLP formation profiles. Average values are $\tau = 31.9 \pm 14$ min, $\tau_1 = -5.5 \pm 4.1$ min, $\tau_2 = 23.7 \pm 11$ min, and $\tau_3 = 2.54 \pm 11$ min. To see this figure in color, go online.

Parameter estimation

Maximum likelihood estimation can be used to estimate the three unknown parameters A, B, and τ_1 of Eq. 10 (32). This method selects values of the parameters that give the experimental data the greatest probability under the assumption that the error ε_i has a normal distribution with mean zero and variance σ^2. Under this assumption, maximum-likelihood estimation is equivalent to least-squares regression, so we use a nonlinear, least-squares curve-fitting routine in the software MATLAB (The MathWorks, Natick, MA) to determine our parameter values and estimate σ as the square-root of the sum of the squares of the errors divided by the length of the data set. We use these parameter estimates to calculate the log-likelihood estimate of Eq. 10.

The likelihood ratio test is then used to compare two nested models to determine which model is more likely to produce the experimental data (33). The first model that we derived in Eq. 10 does not include any parameters that describe the pauselike behavior in the experimental data. To use the likelihood ratio test we add two unknown parameters to Eq. 10 to describe a single pause in the data. The parameter $\tau^1{}_P$ defines the starting time of the pause and the parameter p_1 defines the length of the pause. We assume that the parameter B does not change due to the pause. The second model can be defined piecewise as

$$I(t) = \begin{cases} 0 \quad \text{if} \quad t \le \tau_1 \\ \frac{A}{2}(1-\cos(B(t-\tau_1))) \quad \text{if} \quad \tau_1 < t < \tau_P^1 \\ \frac{A}{2}\left(1-\cos\left(B\left(\tau_P^1-\tau_1\right)\right)\right) \quad \text{if} \quad \tau_{\mathrm{P}}^1 \le t \le \tau_P^1 + p_1 \\ \frac{A}{2}(1-\cos(B(t-p_1-\tau_1))) \quad \text{if} \quad \tau_{\mathrm{P}}^1 + p_1 < t < \tau_P^2 \\ \frac{A}{2}\left(1-\cos\left(B\left(\tau_P^2-\tau_1\right)\right)\right) \quad \text{if} \quad \tau_{\mathrm{P}}^2 \le t \le \tau_P^2 + p_2 \\ \frac{A}{2}(1-\cos(B(t-p_1-p_2-\tau_1))) \quad \text{if} \quad \tau_{\mathrm{P}}^2 + p_2 < t < \frac{\pi}{B} + p_1 + p_2 + \tau_1 \\ A \quad \text{if} \quad t \ge \frac{\pi}{B} + p_1 + p_2 + \tau_1. \end{cases} \tag{11}$$

We use the log-likelihood estimate for Eqs. 10 and 11 to calculate the test statistic. The test statistic is equal to twice the difference in the log-likelihood estimates of the two models. To adjust for multiple comparisons, we use the Bonferroni correction. We reject the null model when $p < 0.05/n$, where n is the number of data sets we compare.

We now consider a final case, which adds two additional unknown parameters to Eq. 11 to describe two pauses in the data. The parameter $\tau^2{}_P$ defines the starting time of the second pause and the parameter p_2 defines the length of the second pause. Again, we assume that the parameter (B) does not change due to either pause. The third model can be defined piecewise as

$$I(t) = \begin{cases} 0 \quad \text{if} \quad t \le \tau_1 \\ \frac{A}{2}(1-\cos(B(t-\tau_1))) \quad \text{if} \quad \tau_1 < t < \tau_P^1 \\ \frac{A}{2}\left(1-\cos\left(B\left(\tau_P^1-\tau_1\right)\right)\right) \quad \text{if} \quad \tau_P^1 \le t \le \tau_P^1 + p_1 \\ \frac{A}{2}(1-\cos(B(t-p_1-\tau_1))) \quad \text{if} \quad \tau_P^1 + p_1 < t < \tau_P^2 \\ \frac{A}{2}\left(1-\cos\left(B\left(\tau_P^2-\tau_1\right)\right)\right) \quad \text{if} \quad \tau_P^2 \le t \le \tau_P^2 + p_2 \\ \frac{A}{2}(1-\cos(B(t-p_1-p_2-\tau_1))) \quad \text{if} \quad \tau_P^2 + p_2 < t < \frac{\pi}{B} + p_1 + p_2 + \tau_1 \\ A \quad \text{if} \quad t \ge \frac{\pi}{B} + p_1 + p_2 + \tau_1. \end{cases} \tag{12}$$

The curve-fitting routine in the software MATLAB may not be able to clearly distinguish between two distinct pauses or one long pause that was broken into two consecutive pauses. To avoid nonidentifiability of ${\tau^1}_P$ and ${\tau^2}_P$, we alter the routine to estimate the seven unknown parameters of Eq. 12 using subsets of data. To do this, we first determine the most likely value of an additional pause using only the experimental data before the value ${\tau^1}_P$, as we determined in Eq. 11. We then consider the experimental data after the value ${\tau^1}_P + p_1$ from Eq. 11, and use this data to determine the most likely value of an additional pause. We compute the likelihood estimate associated with these different values to determine which values associated with the additional pause are more likely when paired with the value of ${\tau^1}_P + p_1$ from Eq. 11. Once we have assigned a value to ${\tau^1}_P$, ${\tau^2}_P$, p_1, and p_2 from Eq. 12, we then use the curve-fitting routine in MATLAB to determine the remaining unknown values and calculate the log-likelihood estimate of the third model. We use the likelihood ratio test to compare the third model (Eq. 12) to the other two models (Eqs. 10 and 11).

Restrictions on parameter estimates

To prevent the curve-fitting routine in MATLAB from identifying a pause in the data once an equilibrium has been reached, we restrict the data to only include values where $I(t) < 0.9\,A$. We also prevent the routine from identifying a pause before the start time of the experimental data.

RESULTS

As Gag concentration within the cytosol rises, Gag proteins assemble on the plasma membrane to nucleate the formation of a VLP. These assembly sites become visible between 3 and 7 h post transfection of Gag and Gag-eGFP in HeLa cells. The nucleation starts with a single site on the membrane and culminates in as many as 100–500 sites by 10 h post transfection. Nucleation of each VLP is followed by a period of Gag polymerization that results in increased fluorescence from the VLP on the plasma membrane. The polymerization of Gag is temporarily interrupted by a pause in Gag polymerization in 60% of VLPs; the identification and characterization of these pauses is the focus of this article. Once the polymerization resumes and the VLP is complete, the fluorescence intensity reaches a plateau, implying full assembly of the Gag within the VLP. This plateau is followed by recruitment of ESCRT components to facilitate the release of the VLP.

The Gag filling fraction is defined as the ratio of Gag at the moment of interest to the total Gag incorporated at the end of VLP formation. We measured the Gag filling fraction during each stage of the assembly to understand the dynamics of VLP formation. The intensity of the VLP in TIRF is a function of its number of Gag proteins as well as its azimuthal location within the penetration depth. To determine the amount of Gag incorporated independent of VLP movement, we measured the TIRF intensity of the same VLP under two different penetration depths and used the ratio of these fluorescence signals to deconvolve the relative Gag incorporation in each VLP as explained in Materials and Methods and shown in Fig. 1. To ensure that the fully formed VLPs were analyzed, only those VLPs imaged from their nucleation, and which stayed separated from other VLPs by at least 1 μm, and recruited VPS4 at the end of assembly within the observation window of our microscopy, were included in our analysis (58 spots from seven cells). The experimentally derived relative Gag incorporations were fit by the shell-filling model as explained in the Materials and Methods. The theoretical fit allows the measurement of the Gag filling fraction corrected for the amount of Gag present during nucleation. Our model assumes new Gag proteins are added at the periphery of the formed Gag lattice during the polymerization. We also assume that Gag assembly and curvature creation follow each other; therefore, the periphery of the Gag lattice is assumed to be identical to the periphery of the forming VLP, as shown in Fig. 2 and explained in Materials and Methods. This model has the advantage of having a single rate constant for Gag addition ($B = 3.1 \times 10^{-3} \pm 2 \times 10^{-3}$ radians/s as

defined by Eq. 8a and measured for 58 VLP assembly events). The model was modified to allow incorporation of pauses, as explained in more detail in Materials and Methods.

VLP formation kinetics

Nucleation kinetics

We imaged the assembly of Gag into VLPs on the plasma membrane of HeLa cells. During nucleation, the VLP is composed of a few Gag proteins assembling on the plasma membrane. Our measurements do not have the required signal/noise to pick the exact nucleation event; therefore, we use the extrapolations of the shell-filling model to estimate nucleation kinetics. Based on extrapolations of the shell-filling model, we estimate the Gag filling fraction at the moment in which VLP emerges out of the background to be 12 $\pm$ 10% for the 58 spots analyzed. The nucleation time $\tau_1 = -5.5 \pm 4.1$ min was measured for the 58 VLPs and is defined as the estimated time required for the VLP to nucleate and appear above signal/noise (Fig. 3). The Gag filling fraction is defined using the theoretical fit as the ratio of Gag at the moment of interest to the total Gag assembled within the VLP. This definition allows an estimate of the Gag filling fraction at the first moment in which the VLP gets above signal/noise, as shown in Fig. 3.

Gag polymerization

Once the forming VLP has sufficient signal to rise above background, Gag continues to polymerize until a plateau is reached and VPS4 is recruited to facilitate fission. The position of this plateau is determined by fitting the shell-filling model. Gag polymerization time is therefore determined as the time between the first appearances of the VLP above noise to the moment that maximum Gag filling fraction is achieved as determined by the fit to the shell-filling model. This time is $\tau_2 = 23.7 \pm 11$ min and is measured for all the 58 VLPs (Fig. 3). The average Gag polymerization time for profiles with pauses is 26 $\pm$ 11 min measured for 37 VLPs, whereas the average for profiles with no pause is 20 $\pm$ 9 min measured for 21 VLPs.

Kinetics of recruitment of VPS4

After full assembly of Gag into the VLP, VPS4 is recruited to assist with membrane fission. We have timed the recruitment of VPS4 with respect to the time of maximum Gag filling fraction. The VPS4 recruitment time for profiles with pauses is $\tau_3 = 1.2 \pm 10$ min measured for 37 VLPs, whereas the average recruitment time for profiles with no pause is $\tau_3 = 4.8 \pm 11$ min measured for 21 VLPs. Fig. 3 *E* shows the distribution of τ_3 for all the profiles.

Lifetime of full assembly

Lifetime of full assembly is defined as the time measured from nucleation to the moment of VPS4 recruitment at the end of Gag assembly. This lifetime for profiles with pauses is 33 $\pm$ 14 min measured for 37 VLPs, whereas the average recruitment time for profiles with no pause is 30 $\pm$ 14 min measured for 21 VLPs.

Pauses during HIV VLP formation

In 60% of the observed VLPs, the polymerization of Gag paused for a period longer than 2 min. After this pause the polymerization resumed with kinetics consistent with the shell-filling model. Pauses are distributed between 2 and 20 min with an average of 4 min with a single-exponential distribution and a time constant of 4.7 min (Fig. 4). Our

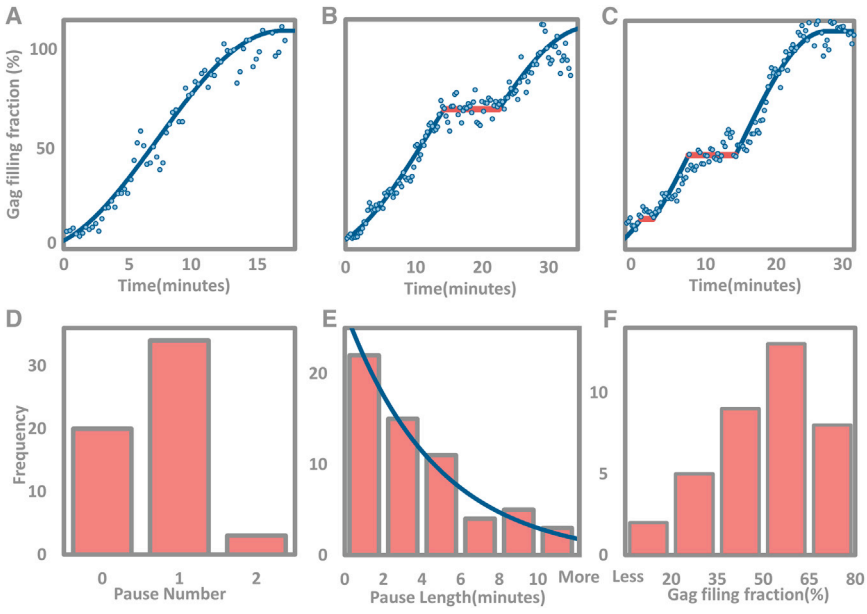

FIGURE 4 Kinetics of pauses. (*A–C*) Three different Gag polymerization behaviors, including no-pause, single pause, and double pause of Gag polymerization. (*Blue dot*) Gag polymerization experimental data; (*blue line*) shell-filling model fitting; and (*dark pink line*) pauses. (*D*) Frequency of three different behaviors. Probability of having a single pause is 60%, double pause is 5%. (*E*) Histogram of pause length in minutes. (*Dark blue line*) Single-exponential distribution with a time constant of 4.7 min. (*F*) Histogram of Gag filling fraction in pause (%). Note that we cannot efficiently detect pauses below 20% filling fraction. To see this figure in color, go online.

signal/noise at the initial stages of assembly is limited, and therefore we cannot detect any pauses below 20% of Gag filling fraction.

We examined the associated Gag filling fractions of 40 pauses from 37 profiles. If pauses occur at a particular curvature or specific number of Gag molecules, then Gag filling fraction during the pause will identify the critical curvature or amount of Gag that generate pauses. Fig. 4 shows the distribution of the observed pauses with respect to the Gag filling fraction, and although pauses between 40 and 60% Gag filling fraction are slightly more prevalent, pauses can happen anywhere along the filling fraction.

If the pauses during formation of VLPs occur independently, double and triple pauses would be common. We have identified 5% (three out of 58) VLPs with a double pause as shown in Fig. 4. Because the probability of having a single pause longer than 2 min is 60%, an independent model predicts the probability of two pauses longer than 2 min as 36%.

The observed 5% double-pause probability is significantly below this ratio, indicating that the incorporation of a single pause may reduce the probability of incorporating a second pause within the VLP. We add that our method is only sensitive to pauses that are longer than 2 min, and therefore we cannot exclude the presence of short pauses ($<$2 min) in addition to the observed long pauses. In addition, we cannot detect pauses that occur near each other or near the beginning or end of VLP formation, making it possible that the deficit of double pauses is due to limited detection power.

Pauses are independent of Gag late domains

To test whether the pauses are caused by interactions of Gag with members of the ESCRT pathway, we repeated our experiments using Gag mutants with double mutations (mutations deleting the PTAP and YPXL motifs that serve to mediate the interactions with two major ESCRT proteins Alix and TSG101). The results from the study of these mutants are shown in the Supporting Material and Fig. S5. For the mutant data average, values are τ_1 (nucleation time) $= -11.36 \pm 9.13$ min and τ_2 (polymerization time) $= 25.75 \pm 17.29$ min. The fraction of profiles with a pause is 71% (see Fig. S5 *D*). The average pause length is 6.04 ± 3.47 min (see Fig. S5 *E*). These data suggests that there is no significant change in either the percentile of profiles with pauses and or the average length of the pauses, and that the pause mechanism is independent of interactions with the ESCRT pathway.

The effect of Gag concentration on the assembly kinetics

The cytosolic concentration of Gag within the cell increases during the 1.5 h imaging window. We have analyzed the rate of assembly (B), VLP lifetime (τ), and pause length from single cells, as shown in Fig. 5. We analyzed the distribution of these parameters for VLPs that formed within the first 45 min of the acquisition, therefore ensuring all of the events recruited VPS4 by the end of the 1.5 h imaging period. We found that the rate of assembly (B) increased from 1.4×10^{-3} radians/s during the first 10 min to 0.0034 radians/s for VLPs starting between 30 and 40 min into the acquisition. Similarly, the lifetime of the VLPs decreased from 42 to 27 min between the same period. This result is in agreement with similar observations from Jouvenet et al. (19). The pause length remains surprisingly constant during the 1.5 h of observation, therefore suggesting that the pauses are not dependent on Gag concentration.

DISCUSSION

Here we report our measurements of polymerization of Gag into fully formed VLPs. Our measurements on kinetics of VLP formation are consistent with previous results. In experiments reported by Baumgärtel et al. (21), where the

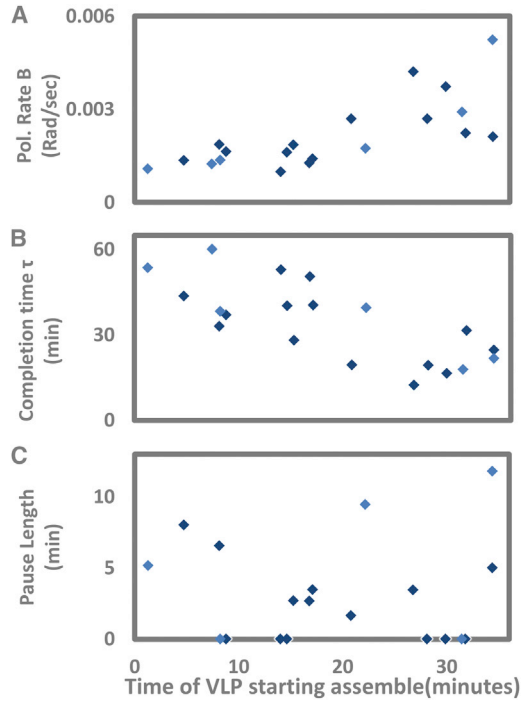

FIGURE 5 Dependence on Gag concentration. During the 90-min period of experimental imaging, the Gag concentration in the cytoplasm is increasing. An analysis of parameters versus the VLP first-appearance time would inherently show the dependence of the parameters to the Gag concentration. (*Dark-* and *medium-blue symbols*) Data for two different cells. (*A*) The plot shows polymerization rate from panel *B* versus time of the VLP formation during the imaging period. The rate of polymerization increases with the concentration of Gag as expected. (*B*) The VLP formation time drops with the increasing Gag concentration. (*C*) The probability of a pause or the pause length is not changed during the observation period in the same cells. To see this figure in color, go online.

VLP formation was observed in cells for a duration of 90 min, the VPS4 spikes were observed mainly between 20 and 45 min after the initiation of the VLP on the membrane, which is consistent with our observation. Jouvenet et al. (20) reported polymerization time of HIV VLPs as 4–20 min with an average of 12 min. In those experiments, however, the Gag proteins were labeled with the less bright mCherry fluorescent protein and the total acquisition on the cell membrane was 45 min, which can inherently discriminate against longer assembly times.

Our data shows 60% of VLPs paused during Gag polymerization for 2–20 min and that pause lengths are distributed exponentially. The frequency of double-pause events was 5%, much lower than expected if the pauses were independent from one another, although our methods might have lower power to detect double pauses. Pauses within the assembly of Gag can also be seen in data from other laboratories (for example, see Figs. 4c, 5b, and 5d from Jouvenet et al. (20)). However, because the data of Jouvenet et al. were acquired using single-penetration-depth TIRF, the presence of the pauses in fluorescence intensity could not be directly linked to pauses in the incorporation of molecules. Our method of imaging based on dual-penetration-depth TIRF microscopy allows the direct measurement of Gag incorporation and identification of pauses within the HIV Gag VLP assembly.

The pauses in the Gag assembly show that polymerization of Gag does not always proceed perfectly and there is a kinetic defect during the VLP assembly. Given that the VLP is assembled by polymerization of thousands of molecules, it is peculiar that polymerization would come to an abrupt stop and then resume a few minutes later. The exponential distribution of pause durations indicates that the VLP assembly is halted waiting for a single event.

Assembly of the VLP is a complex event orchestrated by polymerization of Gag, deformations in the plasma membrane, and possibly interactions with cellular factors during the assembly. One can either expect the pause to be caused by defects directly related to Gag-Gag interactions during polymerization or that the defect can be caused by a failure of interaction between Gag and the cellular machinery involved during VLP assembly.

Although there are many possible events that can cause this particular behavior, we propose the following two models to suggest possible culprits in pause formation:

Model 1: lattice stress is relieved through incorporation of defects during pauses

The Gag lattice in immature HIV virions is formed through hexagonal Gag assemblies covering the internal membrane of the VLP. Because hexagons cannot cover a curved surface, defects incorporate within this lattice, allowing for the closure of the VLP. Incorporation of a defect relieves the stress within the lattice and allows the closure of the VLP. Assuming that Gag polymerization is a Brownian ratchet (34), addition of new Gag molecules to the lattice is limited by the Brownian fluctuations of the membrane. When a section of the lattice polymerizes as a long-range hexagonal lattice, this Gag lattice will create stress within the VLP and dampen the Brownian movement of the membrane required for assembly of new Gag molecules at the periphery. This results in a pause, waiting for large-enough Brownian movement that will allow incorporation of a big defect. This defect will relax the membrane and allow continuation of the assembly. In this model, once the lattice has been relaxed through incorporation of a pause, the secondary pause becomes less likely, as shown in Fig. 6.

Model 2: an enzymatic event essential for further polymerization

Ubiquitin ligases influence the budding of HIV (24–26). The ubiquitin-dependent budding of Gag is not well understood; it is not clear at what stage of VLP formation the ubiquitin effects play a role and how they contribute to membrane remodeling during VLP formation. Here we propose that the pauses may be caused by temporary shortage of ubiquitin-related enzymatic activity. Once the ubiquitin pathway is better understood, one way to test this hypothesis will be to study the effect of crucial enzymes within the pathway on VLP assembly and pause formation.

CONCLUSION

Our method of imaging based on dual-penetration-depth TIRF microscopy allows the identification of pauses within the HIV Gag VLP assembly. Although VLP formation was

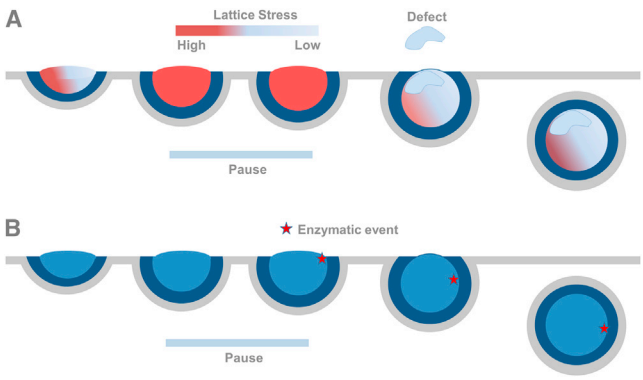

FIGURE 6 Two models for pause formation during Gag polymerization. The mechanism governing the pause is a single stochastic event. We hypothesize that this single event can either be incorporation of a defect that will relax the stress within the curving hexagonal Gag lattice and allow the polymerization to continue (*A*), or evidence of a molecular event such as ubiquitination of Gag that is essential for continuation of polymerization (*B*). Both of these models satisfy the data by providing a single stochastic event that is unique during polymerization. To see this figure in color, go online.

imaged previously, none of the previous studies had the capability to calculate the relative number of added molecules with high-enough sensitivity to demonstrate that the observed pauses in fluorescence intensity were actually due to a pause in assembly versus assembly combined by movement of the VLP out of the TIRF field.

We have observed that the pauses within the assembly of HIV have an exponential distribution with a decay time of 4.7 min. Our signal/noise resolution did not allow quantification of pauses of <2 min; therefore, we cannot rule out the presence of a faster rate of <2 min. The kinetics of pauses are governed through a single rate, which means there is a single stochastic process which has to be overcome for continuation of the VLP assembly.

Expression of Gag within the cytoplasm of host cell is sufficient for assembly of HIV VLPs; however, attempts to reconstruct VLP formation in vitro have not been successful. A simple Gag-centric model of polymerization would predict that assembly of HIV VLPs would proceed uninterrupted, given that the concentration of Gag within the cytosol during assembly is sufficient. The characterized pauses within the assembly of VLP, which occur in the presence of sufficient Gag within the cytosol and in the absence of any interactions with ESCRT components, argue that the assembly is not only limited by Gag availability but also by other cellular or biophysical factors. Proper identification of these elements may be required for reconstructing VLP formation in vitro as well as a complete understanding of the VLP assembly in vivo.

SUPPORTING MATERIAL

Six figures, five equations and supplemental information are available at http://www.biophysj.org/biophysj/supplemental/S0006-3495(13)01123-5.

We thank Dr. Wesley Sundquist for helping us with testing of the VPS4 plasmids and helpful discussions, Dr. James Keener for helpful discussions, Dr. Michael B. Landesman for constructive comments and reading of the manuscript.

This work was supported by National Science Foundation grant No. 1121972 (to S.S.) and a Complex Systems grant from the James S. McDonnell Foundation (to F.R.A.)

REFERENCES

1. Gheysen, D., E. Jacobs, …, M. De Wilde. 1989. Assembly and release of HIV-1 precursor Pr55(Gag) virus-like particles from recombinant baculovirus-infected insect cells. *Cell.* 59:103–112.
2. Briggs, J. A. G., and H.-G. Kräusslich. 2011. The molecular architecture of HIV. *J. Mol. Biol.* 410:491–500.
3. Wright, E. R., J. B. Schooler, …, G. J. Jensen. 2007. Electron cryotomography of immature HIV-1 virions reveals the structure of the CA and SP1 Gag shells. *EMBO J.* 26:2218–2226.
4. Garrus, J. E., U. K. von Schwedler, …, W. I. Sundquist. 2001. Tsg101 and the vacuolar protein sorting pathway are essential for HIV-1 budding. *Cell.* 107:55–65.
5. Martin-Serrano, J., T. Zang, and P. D. Bieniasz. 2001. HIV-1 and Ebola virus encode small peptide motifs that recruit Tsg101 to sites of particle assembly to facilitate egress. *Nat. Med.* 7:1313–1319.
6. Bieniasz, P. D. 2009. The cell biology of HIV-1 virion genesis. *Cell Host Microbe.* 5:550–558.
7. Strack, B., A. Calistri, …, H. G. Göttlinger. 2003. AIP1/ALIX Is a binding partner for HIV-1 p6 and EIAV p9 functioning in virus budding. *Cell.* 114:689–699.
8. Fisher, R. D., H.-Y. Chung, …, C. P. Hill. 2007. Structural and biochemical studies of ALIX/AIP1 and its role in retrovirus budding. *Cell.* 128:841–852.
9. Sundquist, W. I., and H.-G. Kräusslich. 2012. HIV-1 assembly, budding, and maturation. *Cold Spring Harbor Persp. Med.* 2:a006924.
10. Chan, R., P. D. Uchil, …, M. R. Wenk. 2008. Retroviruses human immunodeficiency virus and murine leukemia virus are enriched in phosphoinositides. *J. Virol.* 82:11228–11238.
11. Waheed, A. A., and E. O. Freed. 2009. Lipids and membrane microdomains in HIV-1 replication. *Virus Res.* 143:162–176.
12. Brügger, B., B. Glass, …, H.-G. Kräusslich. 2006. The HIV lipidome: a raft with an unusual composition. *Proc. Natl. Acad. Sci. USA.* 103:2641–2646.
13. Dick, R. A., S. L. Goh, …, V. M. Vogt. 2012. HIV-1 Gag protein can sense the cholesterol and acyl chain environment in model membranes. *Proc. Natl. Acad. Sci. USA.* 109:18761–18766.
14. Ganser-Pornillos, B. K., M. Yeager, and W. I. Sundquist. 2008. The structural biology of HIV assembly. *Curr. Opin. Struct. Biol.* 18:203–217.
15. Ganser, B. K., S. Li, …, W. I. Sundquist. 1999. Assembly and analysis of conical models for the HIV-1 core. *Science.* 283:80–83.
16. Briggs, J. A. G., J. D. Riches, …, H.-G. Kräusslich. 2009. Structure and assembly of immature HIV. *Proc. Natl. Acad. Sci. USA.* 106:11090–11095.
17. Carlson, L.-A., J. A. G. Briggs, …, H.-G. Kräusslich. 2008. Three-dimensional analysis of budding sites and released virus suggests a revised model for HIV-1 morphogenesis. *Cell Host Microbe.* 4:592–599.
18. Ivanchenko, S., W. J. Godinez, …, D. C. Lamb. 2009. Dynamics of HIV-1 assembly and release. *PLoS Pathog.* 5:e1000652.
19. Jouvenet, N., P. D. Bieniasz, and S. M. Simon. 2008. Imaging the biogenesis of individual HIV-1 virions in live cells. *Nature.* 454:236–240.
20. Jouvenet, N., M. Zhadina, …, S. M. Simon. 2011. Dynamics of ESCRT protein recruitment during retroviral assembly. *Nat. Cell Biol.* 13:394–401.
21. Baumgärtel, V., S. Ivanchenko, …, D. C. Lamb. 2011. Live-cell visualization of dynamics of HIV budding site interactions with an ESCRT component. *Nat. Cell Biol.* 13:469–474.
22. VerPlank, L., F. Bouamr, …, C. A. Carter. 2001. Tsg101, a homologue of ubiquitin-conjugating (E2) enzymes, binds the L domain in HIV type 1 Pr55(Gag). *Proc. Natl. Acad. Sci. USA.* 98:7724–7729.
23. Reference deleted in proof.
24. Weiss, E. R., E. Popova, …, H. Göttlinger. 2010. Rescue of HIV-1 release by targeting widely divergent NEDD4-type ubiquitin ligases and isolated catalytic HECT domains to Gag. *PLoS Pathog.* 6:e1001107.
25. Sette, P., J. A. Jadwin, …, F. Bouamr. 2010. The ESCRT-associated protein Alix recruits the ubiquitin ligase NEDD4-1 to facilitate HIV-1 release through the LYPXnL L domain motif. *J. Virol.* 84:8181–8192.
26. Chung, H.-Y., E. Morita, …, W. I. Sundquist. 2008. NEDD4L overexpression rescues the release and infectivity of human immunodeficiency virus type 1 constructs lacking PTAP and YPXL late domains. *J. Virol.* 82:4884–4897.
27. Morita, E., V. Sandrin, …, W. I. Sundquist. 2011. ESCRT-III protein requirements for HIV-1 budding. *Cell Host Microbe.* 9:235–242.

28. Saffarian, S., and T. Kirchhausen. 2008. Differential evanescence nanometry: live-cell fluorescence measurements with 10-nm axial resolution on the plasma membrane. *Biophys. J.* 94:2333–2342.

29. Allersma, M. W., M. A. Bittner, …, R. W. Holz. 2006. Motion matters: secretory granule motion adjacent to the plasma membrane and exocytosis. *Mol. Biol. Cell.* 17:2424–2438.

30. Axelrod, D. 2003. Total internal reflection fluorescence microscopy in cell biology. *Biophotonics B Meth. Enzymol.* 361:1–33.

31. Chen, Y., B. Wu, …, J. D. Mueller. 2009. Fluorescence fluctuation spectroscopy on viral-like particles reveals variable Gag stoichiometry. *Biophys. J.* 96:1961–1969.

32. Adler, F. R. 2005. Modeling the Dynamics of Life: Calculus and Probability for Life Scientists. Thomson Brooks/Cole, Belmont, CA.

33. Zar, J. H. 2010. Biostatistical Analysis. Prentice-Hall/Pearson, Upper Saddle River, NJ.

34. Peskin, C. S., G. M. Odell, and G. F. Oster. 1993. Cellular motions and thermal fluctuations: the Brownian ratchet. *Biophys. J.* 65:316–324.